Jelly, T. O. and Busse, A. (2018) Reynolds and dispersive shear stress contributions above highly skewed roughness. *Journal of Fluid Mechanics*, 852, pp. 710-724. (doi:10.1017/jfm.2018.541)

This is the author's final accepted version.

There may be differences between this version and the published version. You are advised to consult the publisher's version if you wish to cite from it.

http://eprints.gla.ac.uk/164495/

Deposited on: 28 June 2018

Reynolds and dispersive shear stress contributions above highly skewed roughness

Thomas O. Jelly† and Angela Busse

School of Engineering, University of Glasgow, Glasgow G12 8QQ, UK

The roughness functions induced by irregular peak- and/or pit-dominated surfaces in a fully-developed turbulent channel flow are studied by direct numerical simulation. A surface generation algorithm is used to synthesise an irregular Gaussian heightmap with periodic boundaries. The Gaussian heightmap is decomposed into "pits-only" and "peaks-only" components which produces two additional surfaces with similar statistical properties, with the exception of skewness, which is equal and opposite ($\mathcal{S} = \pm 1.6$). While the peaks-only surface yields a roughness function comparable to that of the Gaussian surface, the pits-only surface exhibits a far weaker roughness effect. Analysis of results is aided by deriving an equation for the roughness function which quantitatively identifies the mechanisms of momentum loss and/or gain. The statistical contributions of "form-induced" and stochastic fluid motions to the roughness function are examined in further detail using quadrant analyses. Above the Gaussian and peaks-only surfaces, the contributions of dispersive and Reynolds shear stresses show a compensating effect, whereas, above the pits-only surface, an additive effect is observed. Overall, the results emphasise the sensitivity of the near-wall flow with respect to higher-order topographical parameters, which can, in turn, induce significant differences in the roughness function above a peak- and/or pit-dominated surface.

1. Introduction

The mean dynamics of turbulent flow past irregular rough surfaces are of significant fundamental and practical interest. Roughness effects upon turbulent flow have been reviewed by Jiménez (2004) and Flack & Schultz (2014). The principal effect of surface roughness is to increase the mean momentum deficit in the outer flow, relative to a smooth wall. The downward shift of the logarithmic layer is referred to as the roughness function, ΔU^+ (Hama 1954). Surface roughness effects are incorporated into Reynolds-averaged Navier-Stokes (RANS) simulations by modifying the log-law with an additive roughness function (Durbin *et al.* 2001). Accurate predictions of practical rough-wall flows therefore require a detailed understanding of how ΔU^+ varies with both flow conditions and surface topography. Recent experimental campaigns (Flack *et al.* 2016) and numerical simulations (Thakkar *et al.* 2016; Forooghi *et al.* 2017) have identified skewness, $\mathcal{S}$, as a key topographical parameter that influences ΔU^+.

Skewness quantifies the asymmetry of a roughness distribution about its mean plane. Positively skewed surfaces are peak-dominated, whereas negatively skewed surfaces are pit-dominated. In the early stages of erosion and fouling, an initially smooth surface can become blemished by a random distribution of roughness pits and/or peaks. Examples include the ablation of freshly cast turbine blades (Bons *et al.* 2001) and the onset of bio-fouling on submerged bodies (Monty *et al.* 2016). Many fluid dynamic properties of

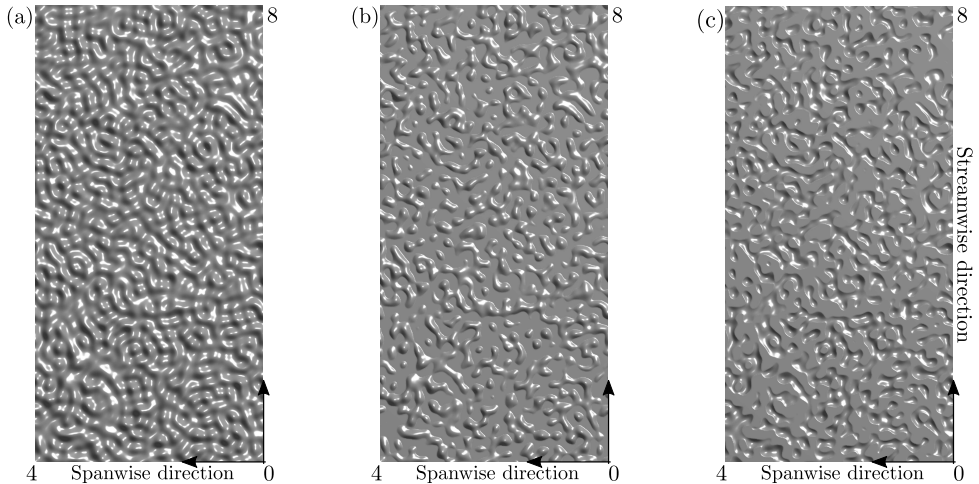† Email address for correspondence: thomas.jelly@glasgow.ac.uk

FIGURE 1. Roughness topographies including: (a) Gaussian; (b) peaks-only and (c) pits-only surfaces. Each surface is generated on an $(8 \times 4)/\delta$ tile, where δ is the mean channel half-height.

irregular pit- and peak-dominated surfaces remain unclear. For example, the relative importance of "form-induced" dispersive stresses and Reynolds stresses, and their respective contributions to ΔU^+, have yet to be considered in detail.

The present study details results from a numerical experiment specifically designed to examine the roughness functions of three irregular surfaces: (i) a Gaussian surface; (ii) a "peaks-only" surface and (iii) a "pits-only" surface. Surface (i) is synthesised using a surface generation algorithm, whereas (ii) and (iii) are obtained from a decomposition of (i). Each roughness topography is shown in figure 1. Analysis of results is aided by deriving an equation for ΔU^+ which quantitatively identifies the mechanisms of mean momentum loss and/or gain for each surface. This paper is organised into four sections. Section 2 outlines the numerical methodology. Results are presented in Section 3. Finally, in Section 4, the conclusions of this work are given.

2. Numerical methodology

Direct numerical simulations (DNS) of rough-wall fully-developed turbulent channel flows are conducted using a variant of the methodology devised by Busse *et al.* (2015).

2.1. *Surface generation algorithm*

Surface heightmaps were generated by correlating the elements of Gaussian random number matrices using a moving average (MA) process. This method of surface generation was devised by Patir (1978) and has been extended here with periodic boundary conditions. A periodic Gaussian heightmap, h_{ij}, of size $N_1 \times N_2$, was generated by evaluating the linear transformation

$$h_{ij} = \sum_{k=1}^{n_1} \sum_{l=1}^{n_2} \alpha_{kl} \eta_{rs} \qquad \begin{aligned} & i = 1, 2, \ldots, N_1 \\ & j = 1, 2, \ldots, N_2 \\ & r = [i + k - 1 \ (\mathrm{mod}\ N_1)] + 1 \\ & s = [j + l - 1 \ (\mathrm{mod}\ N_2)] + 1 \end{aligned} \qquad (2.1)$$

where η_{ij} is a matrix of uncorrelated Gaussian random numbers, α_{kl} are a set of coefficients that give a specified autocorrelation coefficient function (ACF), mod denotes the modulo operator and where $n_1 \times n_2$ is the dimension of the MA window.

The MA coefficients α_{kl} are determined by solving the system of non-linear equations

$$R_{pq} = \sum_{k=1}^{n_1-p} \sum_{l=1}^{n_2-q} \alpha_{kl}\alpha_{k+p,l+q}, \qquad \begin{aligned} p &= 0,1,\ldots,n_1-1 \\ q &= 0,1,\ldots,n_2-1 \end{aligned} \qquad (2.2)$$

using the Newton-based method outlined by Patir (1978), where R_{pq} is the discrete ACF. The Gaussian heightmap is generated with an isotropic exponential ACF

$$R\left(\Delta x_1, \Delta x_2\right) = \exp\left(-2.3\sqrt{\left(\frac{\Delta x_1}{\Delta x_1^*}\right)^2 + \left(\frac{\Delta x_2}{\Delta x_2^*}\right)^2}\right) \qquad (2.3)$$

where $(\Delta x_1, \Delta x_2)$ denote the spatial separations in the streamwise and spanwise directions, respectively, and where $(\Delta x_1^*, \Delta x_2^*)$ denote the spatial separations at which the streamwise and spanwise ACF profiles reduce to 10% of their values at the origin. Further details can be found in the work of Patir (1978).

2.2. *Surface filtering and the pit-peak decomposition*

To obtain a smoothly varying surface from the point cloud, the discrete Gaussian heightmap, h_{ij}, was low-pass Fourier-filtered using the method of Busse *et al.* (2015). After filtering, a "pit-peak" decomposition was applied to the Gaussian heightmap

$$h_{\text{pit}}\left(x_1, x_2\right) = \tfrac{1}{2}h\left(x_1, x_2\right)\left[1 - \text{sgn}\left(h\left(x_1, x_2\right)\right)\right] \qquad (2.4)$$
$$h_{\text{peak}}\left(x_1, x_2\right) = \tfrac{1}{2}h\left(x_1, x_2\right)\left[1 + \text{sgn}\left(h\left(x_1, x_2\right)\right)\right] \qquad (2.5)$$

where h_{pit}, h_{peak} and h denote the pits-only, peaks-only and Gaussian heightmaps, respectively, and where sgn denotes the Signum function.

The pit-peak decomposition of the Gaussian heightmap is shown in figure 1. Statistical properties of each roughness topography are given in table 1. One advantage of the pit-peak decomposition is that h_{pit} and h_{peak} share very similar statistical properties up to fourth order, with the exception of skewness, which is approximately equal and opposite ($\mathcal{S} \approx \pm 1.6$). Compared to a number of recent studies (Flack *et al.* 2016; Thakkar *et al.* 2016; Forooghi *et al.* 2017), the maximum skewness considered in the present study is at least a factor of two higher.

In addition to influencing the level of skewness, the pit-peak decomposition also affects other topographical parameters. For example, the effective slope (ES_x) of the pits- and peaks-only surfaces is a factor of two lower than that of the original Gaussian surface (see table 1). ES_x is defined as the mean absolute streamwise gradient of the heightmap and is known to scale ΔU^+ for a wide range of irregular roughness topographies with symmetric height distributions (Napoli *et al.* 2008; De Marchis *et al.* 2010; De Marchis & Napoli 2012) as well as positively skewed pyramid roughness (Schultz & Flack 2009). Considering that the pits- and peaks-only surfaces share an ES_x of $ES_x < 0.35$ then these surfaces fall into the "waviness flow regime" where ES_x remains an important parameter in scaling the roughness function (Flack & Schultz 2010, 2014). However, in the context of the pits-only surface ($\mathcal{S} \approx -1.6$) and the peaks-only surface ($\mathcal{S} \approx 1.6$), skewness is the key topographical parameter and, as will be shown later, ES_x cannot be relied upon to scale ΔU^+. Irregular surfaces with moderate effective slope are of considerable practical importance, for example a recent surrogate for Nikuradse-type roughness (Thakkar *et al.* 2018) showed a moderate effective slope, which indicates that Nikuradse's sand grain roughness may have been 'wavy' based on the effective slope criterion.

Surface	S_a/δ	S_q/δ	$\mathcal{S}$	$\mathcal{K}$	$\mathcal{L}_{1,corr}/\delta$	$\mathcal{L}_{2,corr}/\delta$	ES_x	ES_y	$S_{z,5\times5}/\delta$	$h_{\max}/\delta$	$\langle h\rangle/\delta$
Gaussian	0.022	0.027	0.03	3.00	0.08	0.08	0.35	0.35	0.167	0.11	0.00
Peaks-only	0.011	0.016	1.62	5.44	0.04	0.04	0.17	0.17	0.085	0.11	0.01
Pits-only	0.011	0.016	-1.64	5.37	0.04	0.04	0.17	0.17	0.085	0.00	-0.01

TABLE 1. Surface statistics including: Mean absolute height (S_a); root-mean-square (RMS) height (S_q); skewness $(\mathcal{S})$; kurtosis $(\mathcal{K})$; streamwise / spanwise correlation length $(\mathcal{L}_{1,corr}, \mathcal{L}_{2,corr})$; streamwise / spanwise effective slope (ES_x, ES_y); mean peak-to-valley height $(S_{z,5\times5})$. The highest roughness crest $(h_{\max})$ and mean height $(\langle h\rangle)$ are also included. Further details of these parameters can be found in work done by Thakkar *et al.* (2016). Note that δ is the mean channel half-height.

Surface	Re_τ	L_1/δ	L_2/δ	Δx_1^+	Δx_2^+	$\Delta x_{3,\min}^+$	$\Delta x_{3,\max}^+$	$T^+ = Tu_\tau^2/\nu$	S_a^+	S_q^+	$h_{\max}^+$
Gaussian	395	8	4	4.94	4.94	0.67	4.5	40000	8.69	10.66	47.78
Peaks-only	-	-	-	-	-	-	-	-	4.35	5.33	47.78
Pits-only	-	-	-	-	-	-	-	-	4.35	5.33	0.00

TABLE 2. Rough-wall simulation parameters including: friction Reynolds number (Re_τ); domain size in the streamwise (L_1) and spanwise (L_2) directions; viscous-scaled grid-spacings including streamwise (Δx_1^+), spanwise (Δx_2^+), minimum wall-normal $(\Delta x_{3,\min}^+)$ and maximum wall-normal $(\Delta x_{3,\max}^+)$ values; viscous-scaled sampling period (T^+); viscous-scaled mean absolute roughness height (S_a^+); viscous-scaled RMS roughness height (S_q^+) and the viscous-scaled highest roughness crest $(h_{\max}^+)$.

2.3. *Direct numerical simulation of turbulent channel flow past irregular rough walls*

DNS of incompressible fully-developed turbulent channel flow past rough walls were performed at a constant mean streamwise pressure gradient using the embedded-boundary algorithm of Busse *et al.* (2015). Three rough-wall simulations were performed with roughness on both the top and bottom walls. A reference smooth-wall simulation was also conducted. The velocity components in the streamwise (x_1), spanwise (x_2) and wall-normal (x_3) directions are u_1, u_2 and u_3, respectively, and p is the fluctuating pressure. The friction Reynolds number is defined here as $Re_\tau \equiv u_\tau\delta/\nu$, where ν is kinematic viscosity, u_τ is the friction velocity and δ is the mean channel half-height of the Gaussian rough-wall configuration. All simulations were conducted at a friction Reynolds number of $Re_\tau = 395$. Viscous-scaled quantities are marked by superscript $+$, e.g. $x_3^+ = x_3 u_\tau/\nu$. The simulation parameters are listed in table 2 and are commensurate with those in recent work related to the current study (Busse *et al.* 2015; Thakkar *et al.* 2016; Busse *et al.* 2017; Thakkar *et al.* 2018).

Statistical quantities are computed using a double-averaged (DA) methodology (Raupach & Shaw 1982). An instantaneous field variable, say a, is decomposed into three parts: (i) a DA component, $\langle\overline{a}\rangle$, where overbar and angled brackets denote successive temporal and planar (x_1, x_2) averages, respectively; (ii) a dispersive component, $\tilde{a}$, and (iii) a stochastic component, a'. The triple decomposition of a is therefore

$$a\left(\mathbf{x}, t\right) = \langle\overline{a}\rangle\left(x_3\right) + \tilde{a}\left(\mathbf{x}\right) + a'\left(\mathbf{x}, t\right) \qquad (2.6)$$

The DA operator is defined as

$$\langle \overline{a} \rangle (x_3) \equiv \frac{1}{\psi(x_3)} \frac{1}{A} \iint\limits_{A} \overline{a}(\mathbf{x}) \, \mathrm{d}x_1 \mathrm{d}x_2 \tag{2.7}$$

where the total area of the wall-parallel plane is $A = L_1 L_2$ and the ratio of the fluid-occupied area, A_f, to the total area is $\psi = A_f(x_3)/A$. In solid-occupied regions, $a(\mathbf{x}, t) = 0$. Note that the DA methodology adopted throughout the present study corresponds to the "intrinsic" averaging procedure discussed in detail by, for example, Nikora *et al.* (2007).

In the DA Navier-Stokes (DANS) equations, the DA dispersive stresses are

$$\langle \tilde{u}_i \tilde{u}_j \rangle = \langle (\overline{u}_i - \langle \overline{u}_i \rangle)(\overline{u}_j - \langle \overline{u}_j \rangle) \rangle \tag{2.8}$$

and the DA Reynolds stresses are

$$\left\langle \overline{u'_i u'_j} \right\rangle = \left\langle \overline{(u_i - \overline{u}_i)(u_j - \overline{u}_j)} \right\rangle \tag{2.9}$$

3. Results

In this section, the roughness functions induced by the Gaussian, peaks-only and pits-only surfaces are examined. Analysis of results is aided by deriving an equation for ΔU^+ which quantifies the contributions of dispersive shear stress (DSS) and Reynolds shear stress (RSS) above each roughness topography.

3.1. *Derivation of the roughness function equation*

The potential sources of momentum loss above a rough surface can be revealed by subtracting the streamwise component of the DANS equation from its smooth-wall counterpart. If the friction Reynolds number is matched between the smooth and the rough-wall case then the difference in total shear stress above the highest roughness crest $(x_3^+ > h_{\max}^+)$ can be written as

$$0 = \Delta \frac{\mathrm{d}\langle \overline{u}_1^+ \rangle}{\mathrm{d}x_3^+} + \langle \tilde{u}_1^+ \tilde{u}_3^+ \rangle_{\mathrm{r}} - \Delta \left\langle \overline{u'_1 u'_3}^+ \right\rangle \tag{3.1}$$

where $\Delta \langle \overline{a}^+ \rangle \equiv \langle \overline{a}^+ \rangle_{\mathrm{s}} - \langle \overline{a}^+ \rangle_{\mathrm{r}}$ denotes the difference between a smooth-wall (subscript "s") and a rough-wall (subscript "r") quantity. For the current cases, the friction Reynolds numbers between the smooth-wall case and the Gaussian case are matched, but there is a small mismatch in the Reynolds numbers of the pits and the peaks cases due to a non-zero mean roughness height $\langle h \rangle$ (see table 1). This leads to an additional error term on the left-hand side of equation 3.1 that is of the order of $|\langle h \rangle|/\delta$ (see derivation in Appendix A). As for the current cases, $|\langle h \rangle|/\delta \ll 1$ and the corresponding mismatch in Re_τ is less than 2%. As a result, the error term can be neglected.

An equation for ΔU^+ can be derived by integrating the total shear stress difference equation 3.1 from the height of the highest roughness crest $h_{\max}^+$ to an arbitrary wall-normal position x_3^+ to obtain

$$\Delta U^+ (x_3^+) = \underbrace{\Delta \langle \overline{u}_1^+ \rangle (h_{\max}^+)}_{\Delta U_s^+} + \underbrace{\int\limits_{h_{\max}^+}^{x_3^+} -\langle \tilde{u}_1^+ \tilde{u}_3^+ \rangle \, \mathrm{d}x_3^+}_{\Delta U_d^+} + \underbrace{\int\limits_{h_{\max}^+}^{x_3^+} \Delta \left\langle \overline{u'_1 u'_3}^+ \right\rangle \mathrm{d}x_3^+}_{\Delta U_t^+} \tag{3.2}$$
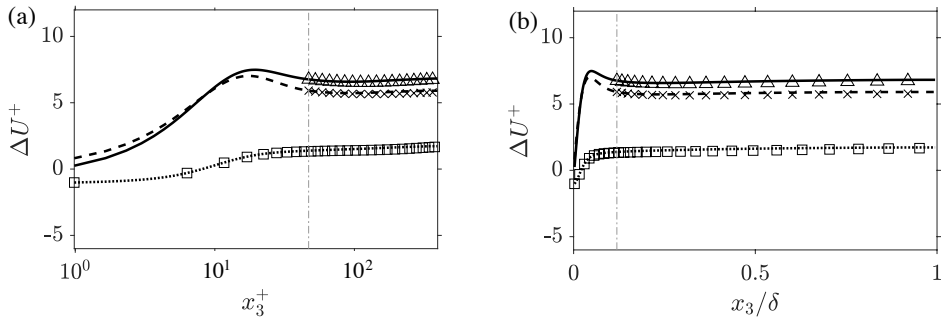
FIGURE 2. Comparison of the roughness function based on the direct evaluation $\Delta U^+ = \langle \overline{u}_1^+ \rangle_{\text{smooth}} - \langle \overline{u}_1^+ \rangle_{\text{rough}}$ (plotted as lines) against ΔU^+ obtained using the roughness function equation 3.2 (plotted as symbols) for the Gaussian ($\boldsymbol{-}, \triangle$), peaks-only ($\boldsymbol{- \ - \ -}, \times$) and pits-only ($\cdots\cdots, \square$) surfaces. The comparison of ΔU^+ is shown in both (a) inner- and (b) outer-scalings. The highest roughness crest of the Gaussian and peaks-only surface is also shown ($\boldsymbol{- \ \cdot \ -}$).

Note that the subscript "r" has been omitted for brevity. The three terms on the right-hand side of the roughness function equation 3.2 have the following interpretation: The first term, ΔU_s^+, represents the difference in streamwise velocity at the highest roughness crest. The second term, ΔU_d^+, represents the integrated effect of the vertical flux of streamwise dispersive momentum. The third and final term, ΔU_t^+, represents the integrated effect of the difference in the vertical flux of streamwise stochastic momentum. MacDonald *et al.* (2016) derived a similar expression for ΔU^+, although their expression does not separate the DSS and RSS difference contributions.

Below the highest roughness crest $(x_3^+ < h_{\max}^+)$, additional pressure gradient and viscous diffusion terms appear on the right-hand side of the DANS equations and arise because the DA operator (equation 2.7) does not commute with wall-normal spatial differentiation if $\psi(x_3) \neq 1$. In equation 3.2, the integrated effect of these additional terms are represented implicitly by term ΔU_s^+. Similar approaches have been adopted by García-Mayoral & Jiménez (2011) and MacDonald *et al.* (2016) in order to decompose ΔU^+ above riblets and sinusoidal roughness, respectively.

The accuracy of the roughness function equation was verified by comparing the wall-normal variation of ΔU^+ from equation 3.2 against the direct evaluation $\Delta U^+ = \langle \overline{u}_1^+ \rangle_{\text{s}} - \langle \overline{u}_1^+ \rangle_{\text{r}}$ for each surface. As shown in figure 2, close levels of agreement are observed at all wall-normal positions. In addition, figure 2 shows that the momentum deficit remains approximately constant from the highest crest to the channel half-height in the presence of peaks. As a result, the roughness function equation 3.2 reduces to $\Delta U^+(\delta^+) \approx \Delta U_s^+(h_{\max}^+)$ for the Gaussian and peaks-only surfaces. Such an approximation does not, however, hold above the pits-only surface. Therefore, whilst the drag force due to the roughness peaks directly generates the momentum deficit in the outer layer, the roughness function induced by the pits-only surface arises due to modifications of the near-wall flow. In order to better understand these differing effects, each term on the right-hand side of the roughness function equation 3.2 can be examined. Herein, all references to ΔU^+ correspond to the centre-line value, $\Delta U^+(\delta^+)$, which agrees well with the downward shift in the log-law (see figure 2a).

3.2. *Analysis of the roughness function equation*

The decomposition of ΔU^+ based on equation 3.2 is shown in figure 3. Positive terms represent a mean momentum loss, whereas negative terms represent a mean momentum
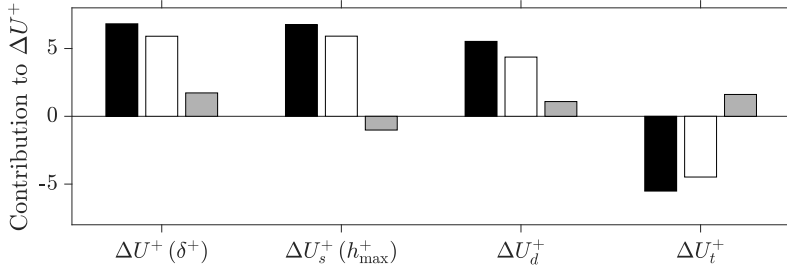
FIGURE 3. Contributions of terms in the roughness function equation 3.2. Data for Gaussian (■), peaks-only (□) and pits-only (▨) surfaces are included for comparison.
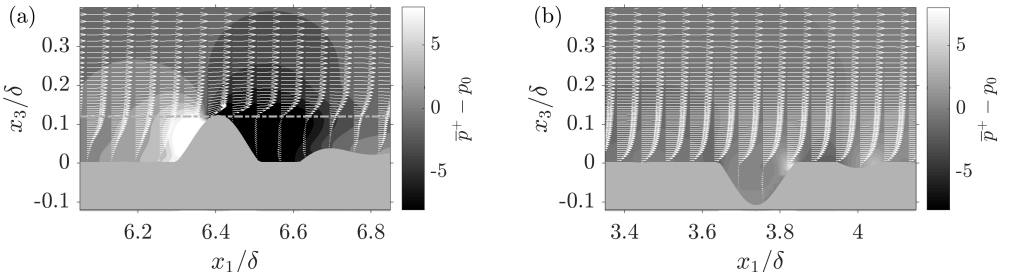

FIGURE 4. Contours of time-averaged pressure, $\overline{p}$, referenced to the mean pressure on the surface, p_0. Spanwise slices intersecting the (a) highest crest of the peaks-only surface and (b) the deepest trough of the pits-only surface are shown. Vectors of the in-plane velocities, $(\overline{u}_1, \overline{u}_3)^+$, and the highest roughness crest of the peaks-only surface (- · -) are also included.

gain. Preliminary observations based on figure 3 include: (i) the roughness functions of the Gaussian surface ($\Delta U^+ = 6.8$) and the peaks-only surface ($\Delta U^+ = 6.0$) are comparable, whereas the pits-only surface yields a far lower value ($\Delta U^+ = 1.7$); (ii) term ΔU_d^+ is positive for all three surfaces, implying that integrated effect of DSS always increases the mean momentum deficit and (iii) the sign of terms ΔU_s^+ and ΔU_t^+ is dependent on the roughness topography, implying fundamental differences in the flow structure above the peak- and pit-dominated surfaces. Overall, figure 3 shows that peaks dominate the roughness effect, whereas pits have relatively little influence.

The sharp reduction of ΔU^+ above the pits-only surface is a consequence of its negative skewness (table 1) which, compared to positively skewed surfaces, give a lower ΔU^+ across a range of friction Reynolds numbers (Flack *et al.* 2016; Busse *et al.* 2017). Other topographical parameters, such as effective slope (ES_x) are known to scale well with ΔU^+. However, despite sharing a common value of ES_x (table 1), the roughness functions of the pits- and peaks-only surfaces differ by 72%. Since ES_x is, by definition, an absolute quantity, it cannot distinguish the sign of an asymmetric roughness distribution and, as a result, cannot explain the difference in ΔU^+ above the peaks- and pits-only surfaces. In this work, differences of ΔU^+ will be clarified by examining each term on the right-hand side of the roughness function equation 3.2.

The first term on the right-hand side of the roughness function equation 3.2 is ΔU_s^+ and represents the streamwise velocity offest at the highest roughness crest. For both the Gaussian and peaks-only surfaces, terms ΔU_s^+ and ΔU^+ match to within 1%, whereas, above the pits-only surface, they differ in both sign and in magnitude (figure 3). To explain the opposing contributions of ΔU_s^+, spanwise slices of the time-averaged pressure field around the highest roughness crest of the peaks-only surface and the deepest
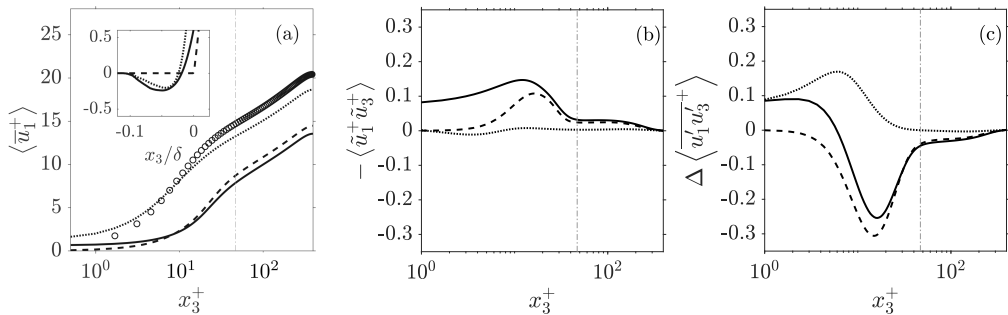
FIGURE 5. DA profiles of (a) streamwise velocity; (b) DSS and (c) RSS difference above the smooth (∘), Gaussian (—), peaks-only (- - -) and pits-only (····) surfaces. The highest roughness crest of the Gaussian and peaks-only surface is also shown (- ·· -).

roughness trough of the pits-only surfaces can be examined. As shown in figure 4, high-pressure regions occur on the windward slopes of surface peaks and the windward lips of surface pits. Low-pressure regions occur downstream of roughness peaks where the flow separates, then reverses, before reattaching upstream. On the other hand, the flow "skims" past the pits, inducing a reverse flow in the lower part of the cavity.

The mean flow patterns shown in figure 4 are reminiscent of those induced by k- and d-type transverse square bar roughness. For example, the flow separation downstream of the highest roughness peak (see figure 4(a)) resembles a k-type scenario (Perry *et al.* 1969; Ikeda & Durbin 2007) whereas the flow reversal within the deepest roughness pit (see figure 4(b)) is similar to a d-type scenario (Leonardi *et al.* 2007). However, considering that the mean flow around transverse square bars is spanwise homogeneous and streamwise phase dependent, drawing a direct comparison against the time-averaged flow properties of irregular, three-dimensional roughness topographies is not straightforward. Therefore, whilst some qualitative understanding can be drawn from figure 4, a quantitative description of the roughness effect induced by the pits- and peaks-only surfaces will focus on DA quantities which make up the roughness function equation 3.2.

The wall-normal variation of DA streamwise velocity above each irregular surface is shown in figure 5(a). A DA reverse flow occurs for the Gaussian and pits-only surfaces at a wall-normal position corresponding to the lower part of the roughness canopy, but is not evident for the peaks-only surface. The magnitude of the reverse flow is on the order of 2% of the centre-line velocity for each surface, which is comparable to past results (Busse *et al.* 2017). At the highest roughness crest of the Gaussian and peaks-only surfaces, ΔU_s^+ makes a positive contribution to ΔU^+ due to integrated effect of losses within the roughness canopy (figure 4(a)). In contrast, for the pits-only surface, the negative contribution of ΔU_s^+ arises due to the DA effect of "skimming" (figure 4(b)) which is manifest as a "slip-velocity" in the mean velocity profile. A similar slip effect occurs for regular d-type roughness geometries whereby the DA effect of stable cavity vortices would result in a streamwise velocity offset (i.e. $\Delta U_s^+ < 0$) at the highest crest (Jiménez 2004).

The second term on the right-hand side of the roughness function equation 3.2 is ΔU_d^+ and represents the integrated effect of "form-induced" momentum transport above the roughness canopy. This term makes a positive contribution to ΔU^+ for each surface (figure 3). Relative to the Gaussian surface, the removal of pits and peaks reduce term ΔU_d^+ by 20% and 80%, respectively, implying that roughness pits are an ineffective source of DSS. The wall-normal variation of DSS is plotted in figure 5(b) and confirms weakened "form-induced" shear stress above the pits-only surface. On the other hand, appreciable
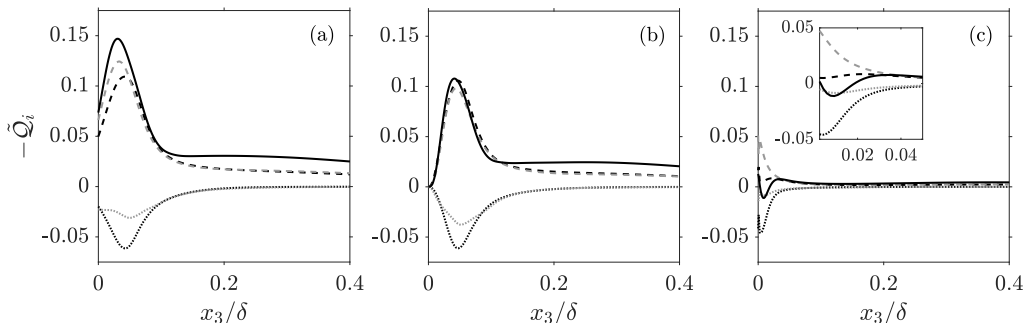
FIGURE 6. Quadrant analysis of DSS showing $\tilde{\mathcal{Q}}_1$ ($\cdots\cdots$); $\tilde{\mathcal{Q}}_2$ (**- - -**); $\tilde{\mathcal{Q}}_3$ ($\cdot\,\cdot\,\cdot$) and $\tilde{\mathcal{Q}}_4$ (- - -) for (a) Gaussian; (b) peaks-only and (c) pits-only surfaces. The sum over all quadrants (—) and the highest roughness crest of the Gaussian and peaks-only surface are also shown (- $\cdot$ -).

levels of DSS are induced within the roughness canopy of the Gaussian and peaks-only surfaces, reflecting the high degree of spatial heterogeneity in the time-averaged flow. Above the highest roughness crest, DSS profiles continue to extend deep into the outer flow before decaying to zero at $x_3/\delta \approx 0.75$. The wall-normal persistence of dispersive stresses has also been noted by Chan *et al.* (2017). In order to associate particular flow events to ΔU_d^+, a quadrant analysis of DSS is performed. Although quadrant analysis is traditionally employed to classify the contributions of flow events to RSS (Wallace *et al.* 1972), it has also been applied to DSS (Pokrajac *et al.* 2007). Considering that $\Delta U_d^+ > 0$ for each surface (figure 3), then the integrated effect of $\tilde{\mathcal{Q}}_2$ ($\tilde{u}_1 < 0, \tilde{u}_3 > 0$) and $\tilde{\mathcal{Q}}_4$ ($\tilde{u}_1 > 0, \tilde{u}_3 < 0$) events are expected to outweigh the combined effect of $\tilde{\mathcal{Q}}_1$ ($\tilde{u}_1 > 0, \tilde{u}_3 > 0$) and $\tilde{\mathcal{Q}}_3$ ($\tilde{u}_1 < 0, \tilde{u}_3 < 0$).

The quadrant decomposition of DSS can be written as

$$\langle \tilde{u}_1^+ \tilde{u}_3^+ \rangle = \sum_{i=1}^{4} \tilde{Q}_i \qquad (3.3)$$

and is plotted in figure 6. As anticipated, $\tilde{\mathcal{Q}}_2$ and $\tilde{\mathcal{Q}}_4$ events dominate $\tilde{\mathcal{Q}}_1$ and $\tilde{\mathcal{Q}}_3$ for the Gaussian and peaks-only surfaces. At the highest roughness crest, $\tilde{\mathcal{Q}}_2$ and $\tilde{\mathcal{Q}}_4$ events are approximately twice that of $\tilde{\mathcal{Q}}_1$ and $\tilde{\mathcal{Q}}_3$ and, beyond $x_3/\delta > 0.25$, activity in odd-numbered quadrants becomes negligible. In contrast, $\tilde{\mathcal{Q}}_2$ and $\tilde{\mathcal{Q}}_4$ events persist in to the outer flow and their respective stress fractions make equal contributions to the local level of DSS. Above the pits-only surface, negligible quadrant activity is observed above $x_3/\delta > 0.1$ and, within closer proximity of the pits, increase $\tilde{\mathcal{Q}}_1$ events are countered by a combined rise of $\tilde{\mathcal{Q}}_2$ and $\tilde{\mathcal{Q}}_4$. However, in a narrow region above the pits ($0.002 < x_3/\delta < 0.018$), odd-numbered activity dominates and, as a result, DSS becomes negative (see inset in figure 6(c)). From a modeling perspective, negative DSS may complicate the application of eddy diffusivity techniques to DANS-type simulations (Manes *et al.* 2008). Overall, however, the integral contribution of negative DSS to ΔU^+ is small and, as a result, term ΔU_d^+ remains positive.

The third and final term on the right-hand side of the roughness function equation 3.2 is ΔU_t^+ and represents the integrated effect of the RSS difference above the roughness canopy. As shown in figure 3, the negative contribution of ΔU_t^+ above the Gaussian and peaks-only surfaces indicates that the integrated effect of RSS is weakened, relative to the smooth-wall value, whereas the positive contribution above the pits-only surface indicates the opposite. The wall-normal variation of RSS difference is plotted in figure 5(c). Negligible differences of RSS are observed in the outer flow ($x_3/\delta > 0.75$) which
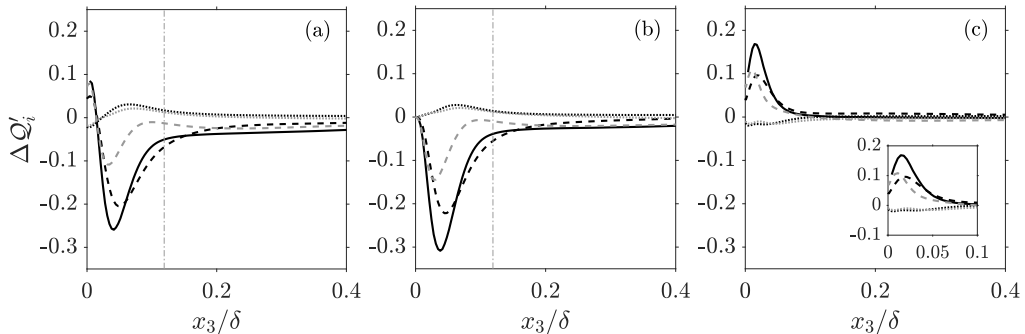
FIGURE 7. Quadrant analysis of RSS difference including $\Delta \mathcal{Q}'_1$ ($\cdots$), $\Delta \mathcal{Q}'_2$ (- - -); $\Delta \mathcal{Q}'_3$ ($\cdots$) and $\Delta \mathcal{Q}'_4$ (- - -) for (a) Gaussian; (b) peaks-only and (c) pits-only surfaces. The sum over all quadrants (—) and the highest roughness crest of the Gaussian and peaks-only surface are also shown (- · -).

is in line with Townsend's outer-layer similarity hypothesis (Townsend 1976). However, as the highest roughness crest of the Gaussian and peaks-only surface is approached, the RSS difference becomes negative. In constrast, above the pits-only surface, the RSS difference is positive below $x_3/\delta < 0.1$. In order to associate particular flow events to ΔU_t^+, the RSS difference is also examined using quadrant analysis.

The quadrant decomposition of RSS difference can be written as

$$\Delta \left\langle \overline{u'_1 u'_3}^+ \right\rangle = \Delta \sum_{i=1}^{4} Q'_i \qquad (3.4)$$

and is plotted in figure 7. Negative values of $\Delta Q'_i$ indicate suppressed quadrant activity, relative to smooth-wall levels, and positive values indicate the opposite. For each surface, the magnitudes of $\Delta Q'_1$ and $\Delta Q'_3$ are small, compared to those of $\Delta Q'_2$ and $\Delta Q'_4$, indicating the relative sensitivity of sweep and ejections events. However, the peaks and pits influence sweep and ejection events in differing manners. For example, at the highest roughness crest of the Gaussian and peaks-only surface, ejection events are suppressed which leads to weakened RSS (figure 5(c)) which, in turn, makes a negative contribution to ΔU^+ through term ΔU_t^+ (figure 3). Above the pits-only surface, both ejections and sweeps are strengthened, which enhances RSS in the near-wall region (figure 5(c)) and, as result, term ΔU_d^+ makes a positive contribution to ΔU^+.

4. Discussion

DNS of turbulent channel flow with irregular rough walls were performed at $Re_\tau = 395$. Three roughness topographies were considered: (i) a Gaussian surface (ii) a peaks-only surface and (iii) a pits-only surface (figure 1). Surfaces (i), (ii) and (iii) gave a ΔU^+ of 6.8, 6.0 and 1.7, respectively, showing the main roughness effect of a non-skewed surface is caused by its peaks. Further analysis of results was aided by evaluating an equation for ΔU^+ which quantitatively identified the mechanisms of momentum loss and/or gain.

The roughness function equation 3.2 indicates that ΔU^+ can be split into three parts: (i) a velocity offset at the highest roughness crest, ΔU_s^+; (ii) the integral effect of form-induced momentum transport, ΔU_d^+ and (iii) the integral effect of the difference in turbulence-induced momentum transport, ΔU_t^+. In the presence of peaks, the approximation $\Delta U^+ \approx \Delta U_s^+$ is valid and terms ΔU_d^+ and ΔU_t^+ have a compensating effect (figure 3). On the other hand, in the absence of peaks, term ΔU_s^+ becomes negative

and this "slip-velocity" effect (figure 5(a)) is offset by positive contributions from both ΔU_d^+ and ΔU_t^+. The reduction of ΔU^+ above the pits-only surface can be attributed to two main factors: (i) suppression of losses due to a slip-type effect (figure 4) and (ii) weakened "form-induced" shear stress due to the absence of peaks (figure 5(b), 6). However, the reduction of ΔU^+ is limited by enhanced Reynolds shear stress, which exceeds smooth-wall levels in the near-wall region (figure 5(c), 7).

Overall, the present study underlines the dependence of the near-wall flow on higher-order topographical parameters, namely skewness. The sensitivity of ΔU^+ with respect to skewness has been confirmed in recent experimental campaigns (Flack *et al.* 2016) and numerical simulations (Forooghi *et al.* 2017). The current study provides a detailed account of the mean-flow mechanisms that determine ΔU^+ above a peak-dominated ($\mathcal{S} = 1.6$) and pit-dominated ($\mathcal{S} = -1.6$) roughness topography. Future work should quantify the Reynolds number dependence of irregular non-Gaussian roughness with the ultimate goal of incorporating topography effects into RANS-type wall models. To this end, minimal-span rough-wall DNS (MacDonald *et al.* 2017) could be used to achieve fully-rough conditions for pit-dominated surfaces which, relative to their peak-dominated counterpart, exhibit a significantly smaller ΔU^+ at the same friction Reynolds number.

Acknowledgements

Appendix A. Effect of mean channel half-height mismatch upon DA momentum difference equations.

The friction velocity, viscous length-scale and friction Reynolds number for a fully-developed smooth-wall turbulent channel flow can be defined as

$$u_{\tau,\mathrm{s}} \equiv \left(-\frac{\delta_{\mathrm{s}}}{\rho}\Pi\right)^{1/2}, \qquad \ell_{\mathrm{s}} \equiv \frac{\nu}{u_{\tau,\mathrm{s}}}, \qquad Re_{\tau,\mathrm{s}} \equiv \frac{\delta_{\mathrm{s}}u_{\tau,\mathrm{s}}}{\nu} \qquad (A\,1)$$

where subscript "s" denotes a smooth-wall quantity. Similar quantities can be defined for a rough-wall turbulent channel flow

$$u_{\tau,\mathrm{r}} \equiv \left(-\frac{\delta_{\mathrm{r}}}{\rho}\Pi\right)^{1/2}, \qquad \ell_{\mathrm{r}} \equiv \frac{\nu}{u_{\tau,\mathrm{r}}}, \qquad Re_{\tau,\mathrm{r}} \equiv \frac{\delta_{\mathrm{r}}u_{\tau,\mathrm{r}}}{\nu} \qquad (A\,2)$$

where subscript "r" denotes a rough-wall quantity.

After defining the ratio of the mean roughness height, $\langle h \rangle$, and the smooth-wall channel half-height, δ_s, as $\epsilon \equiv -\langle h \rangle / \delta_s$, equation A 1 and equation A 2 can be combined to obtain

$$\delta_{\mathrm{r}} = (1+\epsilon)\,\delta_{\mathrm{s}}, \quad u_{\tau,\mathrm{r}} = \left(\sqrt{1+\epsilon}\right)u_{\tau,\mathrm{s}}, \quad Re_{\tau,\mathrm{r}} = \left(\sqrt{1+\epsilon}\right)^3 Re_{\tau,\mathrm{s}}, \quad \ell_{\mathrm{r}} = \frac{1}{\sqrt{1+\epsilon}}\ell_{\mathrm{s}} \, (A\,3)$$

In what follows below, superscript "+" denotes quantities scaled with smooth-wall plus units, i.e. those scaled with ℓ_{s} and $u_{\tau,\mathrm{s}}$ (equation A 1) and superscript "∘" denotes quantities scaled with rough-wall plus units, i.e. those scaled with ℓ_{r} and $u_{\tau,\mathrm{r}}$ (equation A 2). A similar approach has been adopted by MacDonald *et al.* (2016), although their analysis does not separate the DSS and RSS difference contributions.

The DA streamwise momentum balance equations for a smooth-wall turbulent channel flow and a rough-wall turbulent channel flow evaluated above the highest roughness crest can be written as

$$0 = \frac{1}{\delta_s^+} + \frac{d}{dx_{3,s}^+}\left(\frac{d\left\langle \overline{u}_1^+ \right\rangle_s}{dx_{3,s}^+} - \left\langle \overline{u_1' u_3'}^+ \right\rangle_s\right) \tag{A 4}$$

$$0 = \frac{1}{\delta_r^\circ} + \frac{d}{dx_{3,r}^\circ}\left(\frac{d\left\langle \overline{u}_1^\circ \right\rangle_r}{dx_{3,r}^\circ} - \left\langle \overline{u_1' u_3'}^\circ \right\rangle_r - \langle \tilde{u}_1^\circ \tilde{u}_3^\circ \rangle_r\right) \tag{A 5}$$

where the following relationships have been used

$$\frac{1}{\delta_s^+} = \frac{\ell_s}{\delta_s} = \frac{1}{Re_{\tau,s}}, \qquad \frac{1}{\delta_r^\circ} = \frac{\ell_r}{\delta_r} = \frac{1}{Re_{\tau,r}} \tag{A 6}$$

The momentum balance equations A 4 and A 5 can be integrated from an arbitrary wall-normal position to their respective mean channel half-heights to obtain

$$1 - \frac{x_{3,s}^+}{\delta_s^+} = \frac{d\left\langle \overline{u}_1^+ \right\rangle_s}{dx_{3,s}^+} - \left\langle \overline{u_1' u_3'}^+ \right\rangle_s \tag{A 7}$$

$$1 - \frac{x_{3,r}^\circ}{\delta_r^\circ} = \frac{d\left\langle \overline{u}_1^\circ \right\rangle_r}{dx_{3,r}^\circ} - \left\langle \overline{u_1' u_3'}^\circ \right\rangle_r - \langle \tilde{u}_1^\circ \tilde{u}_3^\circ \rangle_r \tag{A 8}$$

After some manipulation, equation A 1 and equation A 2 can be used to recast equation A 8 into "+" units

$$1 - \frac{x_{3,r}^+}{\delta_s^+}\left(\frac{\delta_s}{\delta_r}\right) = \frac{d\left\langle \overline{u}_1^+ \right\rangle_r}{dx_{3,r}^+}\left(\frac{u_{\tau,s}}{u_{\tau,r}}\right)\left(\frac{\ell_r}{\ell_s}\right) - \left\langle \overline{u_1' u_3'}^+ \right\rangle_r\left(\frac{u_{\tau,s}}{u_{\tau,r}}\right)^2 - \langle \tilde{u}_1^+ \tilde{u}_3^+ \rangle_r\left(\frac{u_{\tau,s}}{u_{\tau,r}}\right)^2 \tag{A 9}$$

which can be simplified using equation A 3 to obtain

$$(1 - \epsilon) - \frac{x_{3,r}^+}{\delta_s^+} = \frac{d\left\langle \overline{u}_1^+ \right\rangle_r}{dx_{3,r}^+} - \left\langle \overline{u_1' u_3'}^+ \right\rangle_r - \langle \tilde{u}_1^+ \tilde{u}_3^+ \rangle_r \tag{A 10}$$

We evaluate the difference between the viscous-scaled smooth- and rough-wall cases at equal wall-normal positions, i.e. $x_{3,s}^+ = x_{3,r}^+ = x_3^+$, by subtracting equation A 10 from equation A 7 in order to obtain the momentum balance difference equation

$$\epsilon = \Delta\frac{d\left\langle \overline{u}_1^+ \right\rangle}{dx_3^+} + \langle \tilde{u}_1^+ \tilde{u}_3^+ \rangle - \Delta\left\langle \overline{u_1' u_3'}^+ \right\rangle \tag{A 11}$$

where the left-hand side term shows the effect of a mean channel half-height mismatch. If $\langle h \rangle \neq 0$ then there is an imbalance. However if $|\langle h \rangle| \ll \delta_s$ then the imbalance can be considered negligible. With reference to table 1, the Gaussian surface has a mean roughness height equal to zero ($\langle h \rangle/\delta = 0$) and, as a result, $\epsilon = 0$. On the other hand, the mean roughness heights of the peaks-only surface ($\langle h \rangle/\delta = 0.01$) and the pits-only surfaces ($\langle h \rangle/\delta = -0.01$) are non-zero and therefore $\epsilon \neq 0$. However, since $|\langle h \rangle|/\delta \approx 0.01$ for both the pits- and peaks-only surfaces, the friction Reynolds numbers for these cases agree to within less than 2% of the Gaussian and smooth-wall cases. Therefore, the friction Reynolds numbers of all cases in this study are so close that the effects of mean channel half-height mismatch and the error term ϵ in equation A 11 can be neglected.

REFERENCES

Bons, J. P., Taylor, R. P., McClain, S. T. & Rivir, R. B. 2001 The many faces of turbine surface roughness. *J. Turbomach.* **123** (4), 739–748.

Busse, A., Lützner, M. & Sandham, N. D. 2015 Direct numerical simulation of turbulent flow over a rough surface based on a surface scan. *Computers & Fluids* **116**, 129–147.

Busse, A., Thakkar, M. & Sandham, N. D. 2017 Reynolds-number dependence of the near-wall flow over irregular rough surfaces. *J. Fluid Mech.* **810**, 196224.

Chan, L., MacDonald, M., Chung, D., Hutchins, N. & Ooi, A. 2017 Analysis of the coherent and turbulent stresses of a numerically simulated rough wall pipe. In *J. Phys. Conf. Ser.*, , vol. 822, p. 012011. IOP Publishing.

De Marchis, M. & Napoli, E. 2012 Effects of irregular two-dimensional and three-dimensional surface roughness in turbulent channel flows. *Int. J. Heat Fluid Flow* **36**, 7–17.

De Marchis, M., Napoli, E. & Armenio, V. 2010 Turbulence structures over irregular rough surfaces. *J. Turbul.* **11**, N3.

Durbin, P. A., Medic, G., Seo, J. M., Eaton, J. K. & Song, S. 2001 Rough wall modification of two-layer k- ε. *J. Fluids Eng.* **123** (1), 16–21.

Flack, K. A. & Schultz, M. P. 2010 Review of hydraulic roughness scales in the fully rough regime. *Journal of Fluids Engineering* **132** (4), 041203.

Flack, K. A. & Schultz, M. P. 2014 Roughness effects on wall-bounded turbulent flows. *Phys. Fluids* **26** (10), 101305.

Flack, K. A., Schultz, M. P., Barros, J. M. & Kim, Y. C. 2016 Skin-friction behavior in the transitionally-rough regime. *Int. J. Heat Fluid Flow* **61**, 21–30.

Forooghi, P., Stroh, A., Magagnato, F., Jakirlic, S. & Frohnapfel, B. 2017 Towards a universal roughness correlation. *ASME J. Fluids Eng.* **139** (12), 12121.

García-Mayoral, R. & Jiménez, J. 2011 Hydrodynamic stability and breakdown of the viscous regime over riblets. *J. Fluid Mech.* **678**, 317–347.

Hama, F. R. 1954 Boundary layer characteristics for smooth and rough surfaces. *Trans. Soc. Nav. Arch. Marine Engrs.* **62**, 333–358.

Ikeda, T. & Durbin, P. A. 2007 Direct simulations of a rough-wall channel flow. *J. Fluid Mech.* **571**, 235–263.

Jiménez, J. 2004 Turbulent flows over rough walls. *Annu. Rev. Fluid Mech.* **36**, 173–196.

Leonardi, S., Orlandi, P. & Antonia, R. A. 2007 Properties of d-and k-type roughness in a turbulent channel flow. *Phys. Fluids* **19** (12), 125101.

MacDonald, M., Chan, L., Chung, D., Hutchins, N. & Ooi, A. 2016 Turbulent flow over transitionally rough surfaces with varying roughness densities. *J. Fluid Mech.* **804**, 130–161.

MacDonald, M., Chung, D., Hutchins, N., Chan, L., Ooi, A. & García-Mayoral, R. 2017 The minimal-span channel for rough-wall turbulent flows. *J. Fluid Mech.* **816**, 5–42.

Manes, C., Pokrajac, D., Coceal, O. & McEwan, I. 2008 On the significance of form-induced stress in rough wall turbulent boundary layers. *Acta Geophysica* **56** (3), 845–861.

Monty, J. P., Dogan, E., Hanson, R., Scardino, A. J., Ganapathisubramani, B. & Hutchins, N. 2016 An assessment of the ship drag penalty arising from light calcareous tubeworm fouling. *Biofouling* **32** (4), 451–464.

Napoli, E., Armenio, V. & De Marchis, M. 2008 The effect of the slope of irregularly distributed roughness elements on turbulent wall-bounded flows. *J. Fluid Mech.* **613**, 385–394.

Nikora, V., McEwan, I., McLean, S., Coleman, S., Pokrajac, D. & Walters, R. 2007 Double-averaging concept for rough-bed open-channel and overland flows: Theoretical background. *J. Hydraul. Eng.* **133** (8), 873–883.

Patir, N. 1978 A numerical procedure for random generation of rough surfaces. *Wear* **47** (2), 263–277.

Perry, A. E., Schofield, W. H. & Joubert, P. N. 1969 Rough wall turbulent boundary layers. *J. Fluid Mech.* **37** (2), 383–413.

Pokrajac, D., Campbell, L. J., Nikora, V., Manes, C. & McEwan, I. 2007 Quadrant analysis of persistent spatial velocity perturbations over square-bar roughness. *Exp. Fluids* **42** (3), 413–423.

Raupach, M. R. & Shaw, R. H. 1982 Averaging procedures for flow within vegetation canopies. *Bound.-Layer Meteor.* **22** (1), 79–90.

SCHULTZ, M. P. & FLACK, K. A. 2009 Turbulent boundary layers on a systematically varied rough wall. *Phys. Fluids* **21** (1), 015104.

THAKKAR, M., BUSSE, A. & SANDHAM, N. D. 2016 Surface correlations of hydrodynamic drag for transitionally rough engineering surfaces. *J. Turbul.* **18** (2), 138–169.

THAKKAR, M., BUSSE, A. & SANDHAM, N. D. 2018 Direct numerical simulation of turbulent channel flow over a surrogate for Nikuradse-type roughness. *J. Fluid Mech.* **837**.

TOWNSEND, A. A. 1976 *The Structure of Turbulent Shear Flow*, 2nd edn. Cambridge University Press.

WALLACE, J. M., ECKELMANN, H. & BRODKEY, R. S. 1972 The wall region in turbulent shear flow. *J. Fluid Mech.* **54** (1), 39–48.